This article appeared in ***Opt. Express 33, 41473-41488 (2025)*** and may be found at URL: https://opg.optica.org/oe/fulltext.cfm?uri=oe-33-20-41473###.

Research Article Vol. 33, No. 20 / 6 Oct 2025 / Optics Express 41473
Optics EXPRESS

# Generation depth modeling in time domain diffuse Raman spectroscopy: the homogeneous case

ALESSANDRO BOSSI,[1,2,*,†] VALERIO GANDOLFI,[1,†] ANDREA FARINA,[3] ILARIA BARGIGIA,[1] NASEER KAMMALAMURIYIL,[4] FEDERICO TOMMASI,[4] ANTONIO PIFFERI,[1] AND FABRIZIO MARTELLI[4]

[1]*Dipartimento di Fisica, Politecnico di Milano, Piazza Leonardo da Vinci 32, Milano, Italy*
[2]*Dipartimento di Meccanica, Politecnico di Milano, Via La Masa 1, Milano, Italy*
[3]*Istituto di Fotonica e Nanotecnologie, Consiglio Nazionale delle Ricerche, Piazza Leonardo da Vinci 32, Milano, Italy*
[4]*Dipartimento di Fisica e Astronomia, Universitá degli Studi di Firenze, Via G. Sansone 1, Sesto Fiorentino (Firenze), Italy*
[†]The authors contributed equally to this work
[*]*alessandro.bossi@polimi.it*

**Abstract:** We present a rigorous analytical model, based on the diffusion equation, to calculate the average generation depth of Raman photons in a semi-infinite, diffusive, homogeneous medium, taking into account variations in optical properties between the wavelength of the excitation photons and that of the Raman-scattered photons. The model quantifies how the generation depth depends on photon time-of-flight for time domain diffuse Raman spectroscopy (TD-DIRS) or source-detector distance for spatially offset Raman spectroscopy (SORS). Monte Carlo simulations demonstrate the model's reliability. We applied this model to simulate representative cases of *in vivo* scenarios for which the probed depth is evaluated by the proposed theoretical model. This model provides the basic knowledge to significantly improve the interpretation of SORS and TD-DIRS measurements.



## 1. Introduction

Diffuse Raman Spectroscopy (DIRS) combines the high chemical specificity of Raman scattering with the capabilities of depth probing of diffuse optics to extract information from the deepest parts of the studied medium. Indeed, conventional Raman spectroscopy is commonly limited to the first few hundred of microns of tissues, whereas diffuse optical techniques enable probing deeper layers. Currently, there are four main methods to achieve Raman depth sensitivity: (i) Spatially Offset Raman Spectroscopy (SORS) [1–3] which involves taking multiple measurements at different source-detector distances, where greater separations enable deeper photon penetration; (ii) Frequency Offset Raman Spectroscopy (FORS) [4] which relies on tuning the excitation wavelength thus varying the tissue's optical properties and altering the photon path, which makes it sensitive to different depths; (iii) Transmission Raman Spectroscopy (TRS) [5,6], i.e., a special case of SORS, which works in a transmittance configuration, however is unable to discern different depths; (iv) Time Domain Diffuse Raman Spectroscopy (TD-DIRS) [7–9], which exploits the principle of time-of-flight, where early photons encode information from the surface and late photons encode information from depth.

Indeed, the measurement of Raman spectra from several millimeters up to a few centimeters of depth, non invasively, has recently become a precious diagnostic technique for clinical applications, with particular attention to breast cancer detection [10,11], and bone health [12,13]

#562204 https://doi.org/10.1364/OE.562204
Journal © 2025 Received 17 Mar 2025; revised 28 Jul 2025; accepted 4 Aug 2025; published 22 Sep 2025

Optics EXPRESS

but also for non clinical applications like security, proving the ability to detect concealed elements [14], as well as applications in cultural heritage [15], quality control in pharmaceuticals [5,14,16] and food quality assessment [17].

A better understanding and control of the use of DIRS techniques can be achieved by evaluating the generation depth of the received Raman signal. Although systematic studies on photon penetration depth related to Tyndall diffuse optics - hereafter referred to as Tyndall diffusion/scattering, indicating the elastic scattering of photons in diffusive media - have been proposed since several years [18–21], there is still a lack of an organic theory for Raman signal penetration depth and only a few empirical approaches were presented by Everall et al. [22] and Mosca et al. [23]. More specifically, in the current literature on Diffuse Raman, there are no rigorous general methods for linking the arrival time of the photon (or the source-detector distance in the case of SORS) to the depth at which the Raman scattering events occur.

While in the case of Tyndall elastic scattering, only the statistical concept of maximum and average penetration depth of the detected signal can be defined and investigated [19–21], in diffuse Raman scattering, a further concept of penetration depth is required, that is, the average depth where detected Raman photons are generated, a quantity meaningful only for Raman scattering. In Time Domain Diffuse Raman, this quantity represents the average depth at which detected photons with time-of-flight $t$ underwent wavelength conversion by the Raman scattering interaction, and it yields information about how deep, on average, Raman photons in the material were generated. In this way, the Raman spectrum obtained from photons detected at time $t$ can be directly related to the chemical composition of the Raman molecules present at a specific depth in the medium. This information is therefore crucial for the interpretation of Raman spectroscopy, which cannot be obtained from the pure Tyndall definition of penetration depth.

In this work, we provide a full, comprehensive theory for calculating the generation depth of the Time Domain Diffuse Raman signal at the detector's site when the medium is excited by a unitary source. Although the analysis is carried out in the time domain, it can also be easily extended to the CW domain, for which we provide some examples.

In the following, we will first present the rigorous description of the mean depth of generation of detected Raman photons within the framework of the diffusion approximation (Sec. 2). We developed a model that describes the dependence of the generation depth of Raman photons emitted inside the medium on their arrival time at the detector site by using two coupled diffusion equations as in Ref. [24]. The model takes into account the variation of optical properties with wavelength, as it is required to calculate the Raman signal, and is developed in a semi-infinite geometry, which is typical for various applications. This study has been limited to a homogeneous medium to have a first clear vision of the phenomenon and a better focus on the characteristics of the model. In more complex media (e.g., multilayered or media with localized inclusions), this model is expected to still provide a first-order good approximation. Indeed, even if real tissues may present a layered structure, the assumption of having a background homogeneous medium with average bulk optical properties has been largely employed in tissue spectroscopy [20,25] and can serve very well for the purpose. The results of Monte Carlo (MC) simulations are used as a reference to verify the predictions of the model (Sec. 3). Finally, this solver is used to simulate the generation depth using *in vivo* spectra, deriving the typical [7,8] probed depth in potential biomedical applications (Sec. 4). The solver is openly available on GitHub [29].

## 2. Model

### 2.1. Definitions of depths and physical meaning

Firstly, we need to clarify some definitions we will use in the following. Indeed, while the same definitions of average and maximum penetration depth given by Martelli et al. in Ref. [19] apply to excitation photons; in the case of Diffuse Raman, it is possible to identify three relevant depths that can be defined concerning the Raman signal.

Optics EXPRESS

The first, and most important one, is the average generation depth of detected Raman photons $z_{Raman}$. In TD-DIRS, this quantity represents the average depth at which detected photons with time-of-flight $t$ have undergone the wavelength conversion by the Raman effect. Thus, for instance, the Raman spectrum obtained from photons time gated at time $t$ could be directly related to the chemical composition of Raman molecules present at depth $z_{Raman}$ in the medium.

Next, we define the average penetration depth of Raman photons $z_{avg,Raman}$ as the average depth reached by Raman photons with time-of-flight $t$ after their generation. This quantity is the most similar to the average depth of Tyndall scattering [19], however, it is less interesting from an experimental point of view because it does not give information about the sample composition.

Finally, the last relevant quantity is the maximum penetration depth of Raman photons, $z_{max,Raman}$ defined as the maximum depth reached on average by detected Raman photons with time-of-flight $t$ after their generation. The depth $z_{max,Raman}$ gives information about how deep the generated Raman photons propagate in the material. A visualization of the three defined quantities is shown in Fig. 1 where the results of MC simulations in a semi-infinite medium emphasize the intrinsic difference delivered by the quantities $z_{Raman}$, $z_{avg,Raman}$ and $z_{max,Raman}$ (for definitions of the optical properties of the medium, refer to the next section).

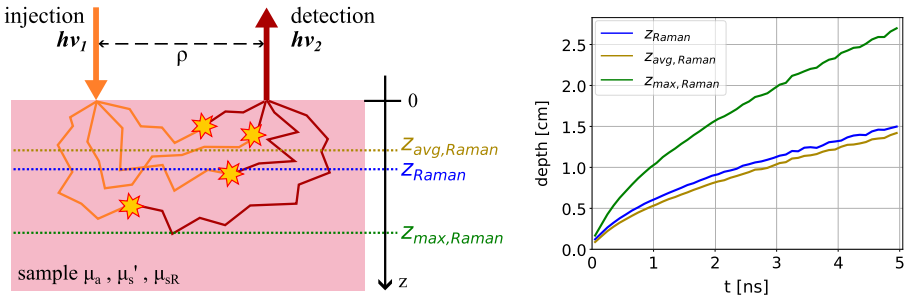


**Fig. 1.** Propagation of photons and relevant penetration depths in Diffuse Raman. The graph refers to the depths calculated with a Monte Carlo simulation in a semi-infinite medium with parameters: $\mu_{ab} = 0.1$ cm$^{-1}$, $\mu'_{sb} = 10$ cm$^{-1}$, $\mu_{ae} = 0.1$ cm$^{-1}$, $\mu'_{se} = 10$ cm$^{-1}$, $\mu_{sR} = 10^{-2}$ cm$^{-1}$, $\rho = 0.5$ cm, $n = 1.4$.

### 2.2. Equations and solutions for photon propagation

We focused our efforts on the derivation of the first quantity, $z_{Raman}$, since it is the most important for the interpretation of Raman measurements. Our model is based on a previous theory of Diffuse Raman developed by Martelli et al. [24]. This description employs two coupled Diffusion Equations (Diffusion Approximation of the Radiative Transfer Equation): the first one describes the fluence $\Phi(\mathbf{r}, t)$ at the position $\mathbf{r} = (x, y, z)$ and time $t$ of excitation photons injected in the material, while the second one describes the fluence $\Phi_e(\mathbf{r}, t)$ of the generated Raman photons at the emission wavelength, i.e.,

$$\left(\frac{1}{v}\frac{\partial}{\partial t} - D\nabla^2 + \mu_a\right)\Phi(\mathbf{r}, t) = q(\mathbf{r}, t), \tag{1a}$$

$$\left(\frac{1}{v_e}\frac{\partial}{\partial t} - D_e\nabla^2 + \mu_{ae}\right)\Phi_e(\mathbf{r}, t) = q_e(\mathbf{r}, t). \tag{1b}$$

The above equations depend on the optical properties of the medium, i.e., absorption coefficient $\mu_a$, diffusion coefficient $D = 1/(3\mu'_s)$ (where $\mu'_s$ is the reduced scattering coefficient), and propagation velocity of photons $v = c/n$ (where $c$ is the velocity of light in vacuum and $n$ is the refractive index of the material). Since the optical properties of the medium depend on

Optics EXPRESS

wavelength and Raman scattering modifies the wavelength of photons, we identify with index $b$ the optical properties at the excitation wavelength and with index $e$ the optical properties at the Raman wavelength. Particular attention is needed for the coefficient $\mu_a$ in the first equation, which is $\mu_a = \mu_{ab} + \mu_{sR}$ to account for the fact that excitation photons are both absorbed by the material and converted by Raman scattering. Thus, $\mu_{sR}$ is a coefficient expressing the probability per unit length that an injected photon is converted by the Raman interaction. The term $q(\mathbf{r}, t)$ represents the source term for the injected excitation photons. In the following, we will consider a unit source, $\delta(\mathbf{r} - \mathbf{r_0})\delta(t)$, i.e., a point-like Delta impulse source at position $\mathbf{r_0} = (0, 0, z_s)$. Finally, the term $q_e(\mathbf{r}, t)$ is the source term of Raman photons; $q_e(\mathbf{r}, t) = \mu_{sR}\Phi(\mathbf{r}, t)$. This term couples the two equations, and its physical meaning is that the source of Raman photons is proportional, via the Raman scattering coefficient, to the distribution of fluence $\Phi(\mathbf{r}, t)$ generated by the excitation photons. The solution of $\Phi_e(\mathbf{r}, t)$ can be obtained by using the Green's function method and is equal to:

$$\Phi_e(\mathbf{r}, t) = (G_e * q_e)(\mathbf{r}, t) = \mu_{sR} \int G_e(\mathbf{r}, \mathbf{r}', t - t')G(\mathbf{r}', \mathbf{r}_0, t')\, d\mathbf{r}'dt', \tag{2}$$

where $G$ and $G_e$ are the Green's functions (DE solutions for unitary sources) for the chosen geometry of the medium for injected photons (excitation wavelength) and generated Raman photons (emission wavelength), respectively. The physical interpretation behind this relation is that the point-like excitation light, which impinges at $\mathbf{r}_0$, diffuses inside the sample, assuming the distribution of the function $G(\mathbf{r}', \mathbf{r}_0, t')$. This light distribution will then be the source for generated Raman photons. Indeed, $G(\mathbf{r}', \mathbf{r}_0, t')$ is evaluated in the position $\mathbf{r}'$, while the same position represents a source point in the function $G_e(\mathbf{r}, \mathbf{r}', t - t')$.

It is possible then to apply to Eq. (2) the relation:

$$R_e(\rho, t) = \frac{\Phi_e(\rho, z = 0, t)}{2A}, \tag{3}$$

which is obtained from the extrapolated boundary partial current (EBPC) condition [26], to retrieve the reflectance $R_e(\rho, t)$, that is the light emitted in all directions out of the medium at a distance $\rho$ ($\rho = \sqrt{x^2 + y^2}$) from the injection point, namely the quantity measured during the experiment. The parameter $A$ depends on the refractive index mismatch between the medium and the external environment, e.g., air. The calculations to retrieve $R_e(\rho, t)$ for a homogeneous semi-infinite medium are shown in Sec. 1 of Supplement 1, and they lead to:

$$\begin{aligned} R_e(\rho, t) = \frac{\mu_{sR}}{32A\pi^2}\sqrt{\frac{vv_e}{DD_e}}\exp\{-\mu_{ae}v_e t\}\int_0^t\int_0^{+\infty}\frac{\exp(-\mu_{sR}vt' - \mu_{ab}vt' + \mu_{ae}v_e t')}{\sqrt{t'(t-t')}(Dvt' + D_e v_e(t-t'))}\times \\ \times\exp\left(-\frac{\rho^2}{4Dvt' + 4D_e v_e(t-t')}\right)\left[\exp\left(-\frac{(z'-z_s)^2}{4Dvt'}\right) - \exp\left(-\frac{(z'+z_s+2z_E)^2}{4Dvt'}\right)\right]\times \\ \times\left[\exp\left(-\frac{(-z')^2}{4D_e v_e(t-t')}\right) - \exp\left(-\frac{(z'+2z_{Ee})^2}{4D_e v_e(t-t')}\right)\right]dz'\,dt'. \end{aligned} \tag{4}$$

The integral in Eq. (4) has no analytical solution. We solved it numerically using the function dblquad from Python package Scipy, which performs integration exploiting the same technique of the QUADPACK Fortran library [27].

### 2.3. Probability density function and average generation depth

Since we are interested in the average generation depth of Raman photons, $z_{Raman}$, following a path similar to the one of Ref. [19], we aim to calculate the probability density function, $f(\bar{z} \mid t)$,

Optics EXPRESS

that a photon with time-of-flight $t$ is emitted at a depth $\bar{z}$:

$$f(\bar{z} \mid t) = \frac{1}{R_e(\rho, t)} \frac{R_e(\bar{z} + \Delta\bar{z} \mid \rho, t) - R_e(\bar{z} \mid \rho, t)}{\Delta\bar{z}} \underset{\Delta\bar{z}\to 0}{=} \frac{1}{R_e(\rho, t)} \frac{\partial R_e(\bar{z} \mid \rho, t)}{\partial \bar{z}}. \tag{5}$$

We point out that in Eq. (5), $R_e(\bar{z} \mid \rho, t)$ represents the contribution to $R_e(\rho, t)$ from Raman sources located at depths smaller than $\bar{z}$. Equivalently, $R_e(\bar{z} + \Delta\bar{z} \mid \rho, t)$ accounts for the Raman generation at depths smaller than $\bar{z} + \Delta\bar{z}$. Thus, we focus on the reflectance that arises from a small depth interval $\Delta z$ centered at $\bar{z} + \frac{\Delta\bar{z}}{2}$ (refer to Fig. 2(a) for a schematic view of the approach). When $\Delta\bar{z} \to 0$ the difference of this term becomes the derivative of $R_e(\bar{z} \mid \rho, t)$ with respect to $\bar{z}$. To ensure physical consistency, the probability density function must be normalized by accounting for the emission contributions across all depths (division by $R_e(\rho, t)$).

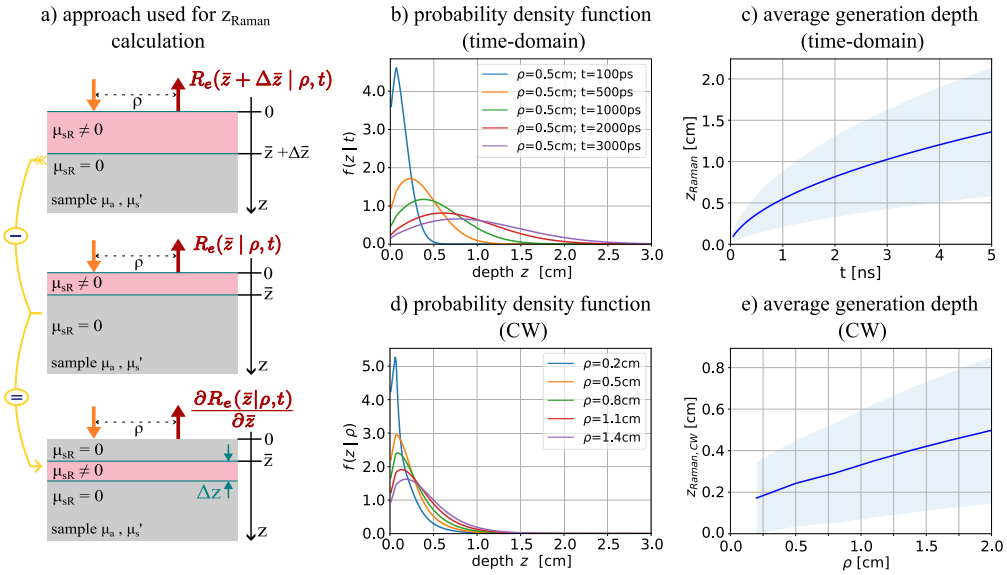


**Fig. 2.** a) schematic of the approach used for the calculation of $z_{Raman}$; b) probability density function $f(\bar{z} \mid t)$; c) average generation depth of detected Raman photons $z_{Raman}(t)$; d) probability density function $f_{CW}(\bar{z} \mid \rho)$; e) average generation depth of detected Raman photons $z_{Raman}(\rho)$. The shaded region represents the standard deviation of the average depth calculated from the variance of the probability density function. The optical properties of the medium are $\mu_{ab} = 0.1$ cm$^{-1}$, $\mu'_{sb} = 15$ cm$^{-1}$, $\mu_{ae} = 0.1$ cm$^{-1}$, $\mu'_{se} = 10$ cm$^{-1}$, $\mu_{sR} = 10^{-5}$ cm$^{-1}$, $n = 1.4$.

Finally, the average generation depth $z_{Raman}$ can be obtained as the average value of the probability density function with respect to depth $\bar{z}$:

$$z_{Raman}(t) = \langle \bar{z} \rangle(t) = \int \bar{z} f(\bar{z} \mid t)\, d\bar{z}. \tag{6}$$

The problem is now shifted to calculating $\frac{\partial R_e(\bar{z}|\rho,t)}{\partial \bar{z}}$ from the equations derived in Sec. 2.2. We note that, using Eq. (2), we can retrieve:

$$\Phi_e(\bar{z} \mid \mathbf{r}, t) = \mu_{sR} \int G_e(\mathbf{r}, \mathbf{r}', t - t') G(\mathbf{r}', \mathbf{r}_0, t') H(\bar{z} - z')\, d\mathbf{r}' dt', \tag{7}$$

where $H(\bar{z} - z')$ is a Heaviside function is used to select only the contributions to the Raman signal given by sources at a depth smaller than $\bar{z}$. This is clear if we consider the Heaviside

Optics EXPRESS

function as part of the term $q_e(\mathbf{r}, t)$: indeed, we are modeling the case in which Raman sources are homogeneously distributed only in the first layer of the medium to depth $\bar{z}$. In the same way, we can write:

$$\Phi_e(\bar{z} + \Delta\bar{z} \mid \mathbf{r}, t) = \mu_{sR} \int G_e(\mathbf{r}, \mathbf{r}', t - t') G(\mathbf{r}', \mathbf{r}_0, t') H(\bar{z} + \Delta\bar{z} - z')\, d\mathbf{r}' dt'. \tag{8}$$

For the calculation of $f(\bar{z} \mid t)$, it is therefore necessary to calculate the difference $R_e(\bar{z} + \Delta\bar{z} \mid \rho, t) - R_e(\bar{z} \mid \rho, t)$, which, because of Eq. (3), will be proportional to $\Phi_e(\bar{z} + \Delta\bar{z} \mid \mathbf{r}, t) - \Phi_e(\bar{z} \mid \mathbf{r}, t)$, that we can retrieve easily from Eq. (7) and Eq. (8). In this calculation, after moving all terms under the same integral and collecting the common parts (see Sec. 2 of Supplement 1), we can note that:

$$\frac{H(\bar{z} + \Delta\bar{z} - z) - H(\bar{z} - z)}{\Delta\bar{z}} \underset{\Delta\bar{z} \to 0}{=} \frac{\partial H(\bar{z} - z)}{\partial \bar{z}} = \delta(z - \bar{z}). \tag{9}$$

Thanks to Eq. (9) it is possible to simplify the following passages because now we can write:

$$\frac{\partial \Phi_e(\bar{z} \mid \mathbf{r}, t)}{\partial \bar{z}} = \mu_{sR} \int G_e(\mathbf{r}, \mathbf{r}', t - t') G(\mathbf{r}', \mathbf{r}_0, t') \delta(z' - \bar{z})\, d\mathbf{r}' dt'. \tag{10}$$

We want to stress that Eq. (10) can be retrieved directly from Eq. (1) with $q_e(\mathbf{r}, t) = \mu_{sR} \Phi(\mathbf{r}, t) \delta(z - \bar{z})$. This clarifies the physical meaning of our approach: the Dirac delta function limits Raman generation to a layer of infinitesimal thickness placed at a fixed depth $\bar{z}$, as schematized in Fig. 2(a). Then it is also straightforward to note that $\frac{\partial \Phi_e(\bar{z} \mid \mathbf{r}, t)}{\partial \bar{z}}$ is the contribution of the Raman-active selected layer to the total fluence $\Phi_e(\mathbf{r}, t)$ and the following relation holds:

$$\Phi_e(\mathbf{r}, t) = \int_0^{+\infty} \frac{\partial \Phi_e(\bar{z} \mid \mathbf{r}, t)}{\partial \bar{z}} d\bar{z}. \tag{11}$$

Now, thanks to Eq. (3), it is possible to retrieve easily $\frac{\partial R_e(\bar{z} \mid \rho, t)}{\partial \bar{z}}$ from $\frac{\partial \Phi_e(\bar{z} \mid \mathbf{r}, t)}{\partial \bar{z}}$ and calculate the probability density function $f(\bar{z} \mid t)$.

The approach used until this point is general and can be adapted to different geometries of the sample according to the Green's function used. Moreover, there are no further approximations except for the validity conditions of the Diffusion Equation and the boundary conditions relating to its use.

The development of our approach in the case of a semi-infinite homogeneous medium is completely shown in Sec. 2 of Supplement 1. In brief, we substitute in Eq. (10) the Green's functions for the semi-infinite medium geometry obtained with the extrapolated boundary conditions [28]. We consider the Green function of the excitation photon $G$ as the source of $G_e$, and so $\mathbf{r}'$ is the source point of $G_e$. We have an integral in three variables $x'$, $y'$, $t'$ (because $z'$ is fixed by the delta function). After solving analytically the parts depending on $x'$ and $y'$ and applying Eq. (3) we get:

$$\begin{aligned} \frac{\partial R_e(\bar{z} \mid \rho, t)}{\partial \bar{z}} = {} & \frac{\mu_{sR}}{32A\pi^2} \sqrt{\frac{v v_e}{D D_e}} \exp\{-\mu_{ae} v_e t\} \int_0^t \frac{\exp\{-\mu_{sR} v t' - \mu_{ab} v t' + \mu_{ae} v_e t'\}}{\sqrt{t'(t - t')}\,[D v t' + D_e v_e (t - t')]} \times \\ & \times \exp\left\{-\frac{\rho^2}{4 D v t' + 4 D_e v_e (t - t')}\right\} \left[\exp\left\{-\frac{(\bar{z} - z_S)^2}{4 D v t'}\right\} - \exp\left\{-\frac{(\bar{z} + z_S + 2 z_E)^2}{4 D v t'}\right\}\right] \times \\ & \times \left[\exp\left\{-\frac{(-\bar{z})^2}{4 D_e v_e (t - t')}\right\} - \exp\left\{-\frac{(\bar{z} + 2 z_{Ee})^2}{4 D_e v_e (t - t')}\right\}\right] dt'. \end{aligned} \tag{12}$$

where $z_S$ is the depth of a unitary isotropic source (we consider $z_S = 1/\mu_s'$ to describe a pencil beam source impinging on the medium perpendicularly at $\rho = 0$ [28]) while $z_E = 2AD$ and $z_{Ee} = 2AD_e$ are the extrapolated boundaries for the Green's functions at the excitation and

Optics EXPRESS

emission wavelengths, respectively. The integral in Eq. (12) has no analytical solution, so it must be solved numerically. For that, we used the function quad from the Python package Scipy [27].

The probability density function $f(\bar{z} \mid t)$ can now be calculated as the ratio of Eq. (12) by Eq. (4) (the complete formula is reported in Supplement 1). To retrieve the example of $f(\bar{z} \mid t)$ shown in Fig. 2(b), we have set $\mu_{ab} = 0.1\ \text{cm}^{-1}$, $\mu'_{sb} = 15\ \text{cm}^{-1}$, $\mu_{ae} = 0.1\ \text{cm}^{-1}$, $\mu'_{se} = 10\ \text{cm}^{-1}$, $\mu_{sR} = 10^{-5}\ \text{cm}^{-1}$, $n = 1.4$, $\rho = 0.5$ cm. The calculation took about 2 minutes on a laptop with 16 GB RAM and an i7-10510U CPU for a time scale with 100 points and a depth scale of 500 points. The code used for computation is available in Ref. [29]. We verified that $\int_0^{+\infty} f(\bar{z} \mid t)\, d\bar{z} = 1$ and thus confirming that $f(\bar{z} \mid t)$ is a probability density function. It can be noted that as the time $t$ increases, the probability distribution shifts towards greater depth values, increasing its dispersion, which means that, as expected, longer times encode greater depths with increasing uncertainty.

From these data we obtained, according to Eq. (6), the average generation depth $z_{Raman}$, shown in Fig. 2(c), which provides immediate information on the depth of the medium from which the detected Raman emission originates. The numerical integration was done with the trapz function from the Scipy Python package, which implements the integration by trapezoidal rule. As expected, the average generation depth is higher for photons with higher time-of-flight $t$: indeed, they have traveled more in the material, thus probing deeper layers. In time domain, both the probability density function and the average generation depth are independent of the source-detector distance $\rho$, as we will show later in Sec. 3.

It is worth noting that Eq. (12) and also the proposed calculation of the average generation depth are rigorous within the validity of the diffusion approximation. Moreover, once the probability density function associated with the Raman generation depth has been obtained, additional quantities such as the median and percentiles can be readily calculated. Although not investigated here, these quantities can be useful for the interpretation of experimental measurements and are listed in Table 1, along with their calculation and physical significance.

**Table 1. Summary of the main relevant quantities that can be derived from the probability density function *f***

| Quantity | Definition | Physical Interpretation |
|---|---|---|
| Mean ($z_{Raman}$) | TD: $\langle z\rangle(t) = \int_0^{\infty} z f(z\|t)\, dz$<br>CW: $\langle z\rangle(\rho) = \int_0^{\infty} z f(z\|\rho)\, dz$ | The average depth at which photons detected with time-of-flight $t$ or source-detector separation $\rho$ have undergone Raman scattering. |
| Variance | TD: $\sigma^2(t) = \int_0^{\infty} (z - \langle z\rangle(t))^2 f(z\|t)\, dz$<br>CW: $\sigma^2(\rho) = \int_0^{\infty} (z - \langle z\rangle(\rho))^2 f(z\|\rho)\, dz$ | The statistical spread of the Raman generation depth of the detected photons at $t$ or $\rho$. |
| Percentile p% ($Z_p$) | TD: $\int_0^{Z_p(t)} f(z\|t)\, dz = \frac{p}{100}$<br>CW: $\int_0^{Z_p(\rho)} f(z\|\rho) dz = \frac{p}{100}$ | The depth below which $p$% of the detected Raman photons generation occurs. |
| Median (50th Percentile) | TD: $Z_{50}(t)$<br>CW: $Z_{50}(\rho)$ | The depth that divides the detected photon population into two equal halves. |
| Measured average depth ($\overline{z_M}$) | TD: $\overline{z_M}(t_0, t_1) = \frac{\int_{t_0}^{t_1} \langle z\rangle(t) R(t) dt}{\int_{t_0}^{t_1} R(t) dt}$<br>CW: $\overline{z_M}(\rho_0, \rho_1) = \frac{\int_{\rho_0}^{\rho_1} \langle z\rangle(\rho) R(\rho) d\rho}{\int_{\rho_0}^{\rho_1} R(\rho) d\rho}$ | The average Raman generation depth measured over a time gate $(t_0, t_1)$ or in CW over a ring between radii $(\rho_0, \rho_1)$. |
| Fractional contribution of depths ($r_{z_1,z_2}$) | TD: $r_{z_1,z_2}(t) = \int_{z_0}^{z_1} f(z\|t) dz$<br>CW: $r_{z_1,z_2}(\rho) = \int_{z_0}^{z_1} f(z\|\rho) dz$ | Fraction of the detected photons at time of arrival $t$, or source-detector $\rho$ originating from depths between $z_0$ and $z_1$. |

### 2.4. Extension to CW case

We want to extend our model to the case in which the source of excitation light is not pulsed as in time domain but constant (continuous wave - CW domain). This is the case of Spatially

Optics EXPRESS

Offset Raman Spectroscopy (SORS) measurements, in which the depth selectivity is given by the source-detector distance instead of the time-of-flight of photons.

A rigorous approach would consist of using the Green's function for the CW case and repeating all the previous calculations. However, it is possible to get the same results by integrating in time, from $t = 0$ to $t = +\infty$, the two terms $R_e(\rho, t)$ and $\frac{\partial R_e(\bar{z}|\rho,t)}{\partial \bar{z}}$ obtained before [20]. Thus, we have the probability density function $f_{CW}(\bar{z} \mid \rho)$ that photons detected at the source-detector distance $\rho$ come from depth $\bar{z}$:

$$f_{CW}(\bar{z} \mid \rho) = \frac{1}{R_{e,CW}(\rho)} \frac{\partial R_{e,CW}(\bar{z} \mid \rho)}{\partial \bar{z}}, \tag{13}$$

where $R_{e,CW}(\rho) = \int_0^\infty R(\rho, t)\, dt$ and $\frac{\partial R_{e,CW}(\bar{z}|\rho)}{\partial \bar{z}} = \int_0^\infty \frac{\partial R_e(\bar{z}|\rho,t)}{\partial \bar{z}}\, dt$.

In this way, we can obtain the value of $z_{Raman}$ for different source-detector distances $\rho$ as:

$$z_{Raman}(\rho) = \langle \bar{z} \rangle(\rho) = \int \bar{z} f_{CW}(\bar{z} \mid \rho)\, d\bar{z}. \tag{14}$$

Fig. 2(d) shows the CW probability density function and average generation depth for a medium with $\mu_{ab} = 0.1$ cm$^{-1}$, $\mu'_{sb} = 15$ cm$^{-1}$, $\mu_{ae} = 0.1$ cm$^{-1}$, $\mu'_{se} = 10$ cm$^{-1}$, $\mu_{sR} = 10^{-5}$ cm$^{-1}$, $n = 1.4$. The calculation was done by retrieving the time domain reflectance for different values of $\rho$ and applying the numerical time integration according to Eq. (13). As expected, the behavior of $f_{CW}(\bar{z} \mid \rho)$ and $z_{Raman}(\rho)$, shown in Fig. 2(e), is similar to their time domain counterparts. The values obtained are also compatible with some results from the recent literature [23].

## 3. Validation using Monte Carlo simulations and results

To better understand the capabilities of our theoretical model presented above, we evaluated the results given by the model for different combinations of $\mu_a$ and $\mu'_s$ values and compared them with Monte Carlo (MC) simulations. They represent a sufficiently reliable method, proven to be equivalent to experimental measurements in many previous studies [23,30–32], that allows us to validate our model.

### 3.1. Monte Carlo code

The Monte Carlo code we used is a modified version of MCML [33,34], previously exploited and described in Ref. [24]. The code is available in Ref. [35]. The photons are injected vertically into a semi-infinite medium (cylinder with a radius of 10 cm) and detected at a distance $\rho$ from the injection point. To simulate Raman scattering, at each propagation step of a photon, a random variable is sampled and the photon is converted with a probability per unit length equal to the Raman scattering coefficient $\mu_{sR}$. We set $\mu_{sR} = 10^{-2}$ cm$^{-1}$, even though it is larger than the typical $10^{-5}$ cm$^{-1}$ value, to speed up the MC simulation. This does not hamper the validity of the comparison because, as we will show later, a variation in $\mu_{sR}$ of many orders of magnitude leads only to a variation of <1% in $z_{Raman}$. After a Raman scattering event occurs, the propagation continues with a different scattering coefficient to account for the change in wavelength. The effect of absorption is applied at the end of the simulation by decreasing the weight of photons according to the Beer-Lambert-Bouguer law by the factor $\exp\{-\mu_{ab}\ell_b - \mu_{ae}\ell_e\}$, where $\ell_b$ and $\ell_e$ are the pathlengths before and after the Raman scattering event, respectively [20,26]. All the simulations carried out for this work consider the Raman-scattering event as isotropic, while other scattering events used the Henyey and Greenstein model with an asymmetry factor $g = 0.8$ [26].

During the MC simulation, the depth of each propagation step and the depth at which Raman conversion occurred are saved. These values are exploited at the end of the simulation to calculate $z_{Raman}$, $z_{avg,Raman}$ and $z_{max,Raman}$ by a weighted average of the received trajectories. Figure 1

Optics EXPRESS

shows the behavior of these different depth types, calculated from MC simulation, as a function of time, in a semi-infinite medium. The complete results with different optical properties can be found in Sec. 3 of Supplement 1. It can be seen that, as expected from the Tyndall model [19], $z_{avg,Raman}$ is about half of $z_{max,Raman}$. Further, $z_{Raman}$ is larger but not far from the values of $z_{avg,Raman}$. These results satisfy the physical expectation of photon migration, as Raman photons can migrate towards lower depths after their generation before being detected, thus leading to $z_{avg,Raman}<z_{Raman}$. Only for $\mu_{ab}>\mu_{ae}$ at late times can it be found $z_{Raman}<z_{avg,Raman}$, as in this case, the importance of Raman photons emitted at larger depths, and finally detected after migrating deeper in the medium, is emphasized.

### 3.2. Effect of optical properties and source-detector distance on $z_{Raman}(t)$

We performed some simulations by varying alternatively one coefficient among $\mu'_{sb}$, $\mu_{ab}$, $\mu'_{se}$ and $\mu_{ae}$ keeping fixed the others and covering all the possible cases to see the effect of the optical properties on the average generation depth $z_{Raman}(t)$. Then, with fixed values for the optical properties, we simulated the propagation for different values of source-detector distance $\rho$ and Raman scattering coefficient $\mu_{sR}$ to see the effect of these experimental parameters as well. The results are shown in Fig. 3 where solid lines represent data from MC simulations while dashed lines report the results from our model. The corresponding probability density functions are reported in Sec. 4 of Supplement 1. In Sec. 5 of Supplement 1 we show the standard deviation of $z_{Raman}$ at different $t$, for varying $\mu_{ae}$ and $\mu'_{se}$.

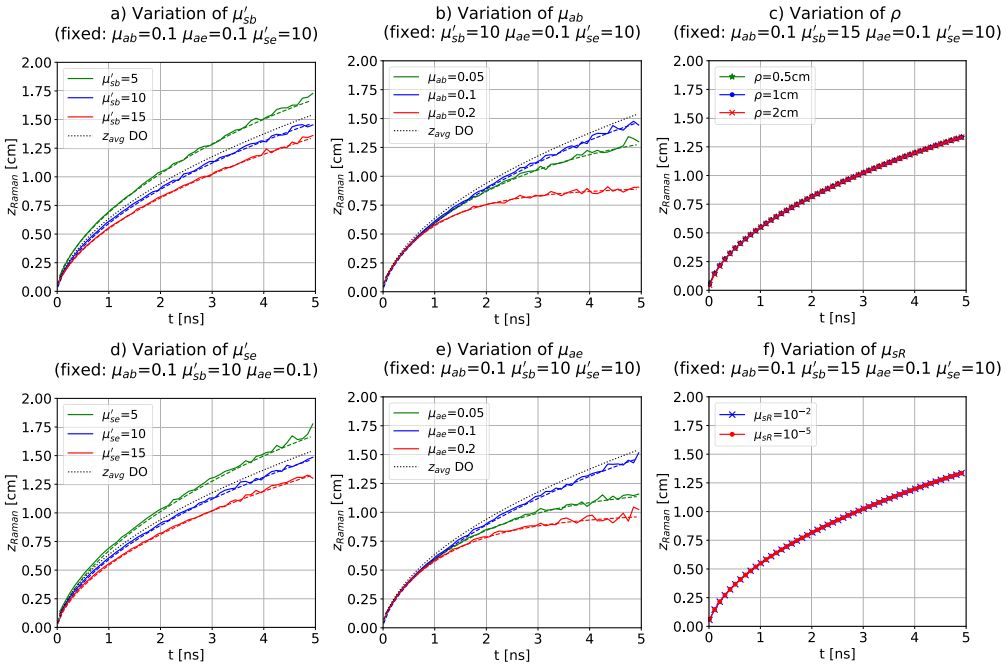


**Fig. 3.** Average generation depth $z_{Raman}$ (TD case) for: a) variation of $\mu'_{sb}$; b) variation of $\mu_{ab}$; c) variation of $\rho$; d) variation of $\mu'_{se}$; e) variation of $\mu_{ae}$; f) variation of $\mu_{sR}$. The unit of optical properties is $cm^{-1}$. Solid lines refer to data from MC simulations, while dashed lines refer to data from the model. The average depth, in the case only the effect of Tyndall scattering at the excitation wavelength is considered [19] (medium with $\mu_a$ = 0.1 $cm^{-1}$ and $\mu'_s$ = 10 $cm^{-1}$), is represented with a black dotted line. The refractive index of the medium and the external one are 1.4 and 1, respectively.

Optics EXPRESS

As a first evaluation of the model, we can compare the behavior of $z_{Raman}$ to the average penetration depth in the case of only Tyndall scattering [19], shown with a black dotted line in each graph in Fig. 3. When the coefficients are set such that $\mu_{ae} = \mu_{ab}$ and $\mu'_{se} = \mu'_{sb}$ the curves are nearly overlapped. This is compatible with the fact that in this situation, since the optical properties for excitation and Raman photons are the same, propagation for both is equivalent, as if Raman scattering were not present. The only difference is in the single Raman scattering event, which is always isotropic ($g = 0$), while Tyndall scattering can also be anisotropic ($g \geq 0$)

Nevertheless, if we consider the more realistic case in which $\mu_{ae} \neq \mu_{ab}$ and $\mu'_{se} \neq \mu'_{sb}$, the average generation depth $z_{Raman}$ becomes different from the average penetration depth foreseen by the model describing only elastic scattering. Raman photons experience different optical properties than excitation photons, so their propagation will be different, and this will affect the depth probed by photons detected at time $t$. In particular, we can note that an increase in the reduced scattering coefficient $\mu'_{se}$ (or $\mu'_{sb}$) leads to a smaller probed depth for the same time-of-flight $t$, in agreement with the fact that, for higher scattering, photons are more spread in the medium and it is more difficult for them to reach higher depths. For example, as shown in Fig. 3(a) at $t = 2$ ns (with $\mu_{ab} = 0.1$ cm$^{-1}$, $\mu_{ae} = 0.1$ cm$^{-1}$, $\mu'_{se} = 10$ cm$^{-1}$), increasing $\mu'_{sb}$ from 5 to 15 cm$^{-1}$ reduces the average depth from 1.0 to 0.8 cm. Instead, the behavior concerning the absorption coefficient is more complex. The maximum depth is reached when $\mu_{ae} = \mu_{ab}$ while a mismatch in absorption coefficient decreases $z_{Raman}(t)$. This can be explained by noting that Eq. (12) shows the difference $\mu_{ae} v_e t' - \mu_{ab} v t'$ that, when $\mu_{ae} \neq \mu_{ab}$, has a significant effect on the calculation of $z_{Raman}(t)$. The physical meaning is that when $\mu_{ae} > \mu_{ab}$ Raman photons generated from deeper layers may be absorbed before reaching the detector, while when $\mu_{ae} < \mu_{ab}$ photons at the excitation wavelength may be absorbed before reaching deeper layers: for both cases, on average we have detected Raman photons generated at smaller depths and thus a lower $z_{Raman}(t)$, especially at higher time-of-flight $t$. As illustrated in Fig. 3(e) (for $t = 2$ ns, with $\mu_{ab} = 0.1$ cm$^{-1}$, $\mu'_{sb} = 10$ cm$^{-1}$, $\mu_{ae} = 0.1$ cm$^{-1}$, $\mu'_{se} = 10$ cm$^{-1}$), the average depth is 0.89 cm when $\mu_{ae} = \mu_{ab} = 0.1$ cm$^{-1}$, but drops to 0.78 cm when $\mu_{ae} = 0.15$ cm$^{-1}$.

From Fig. 3(f) it is possible to observe that $\mu_{sR}$ does not influence $z_{Raman}(t)$ due to its small value compared to the absorption terms. Indeed, this factor only considers the probability of generation of Raman photons, which is independent of their propagation and the depth at which are generated.

Finally, Fig. 3(c) shows that $z_{Raman}(t)$ is completely independent of source-detector distance $\rho$. This behavior is well known in Diffuse Optics [19] and confirms that in time domain measurements the depth information is encoded only by the photon's time-of-flight. A change in $\rho$ will only change the intensity of the signal detected at different times $t$. For example, increasing $\rho$ will lead to a lower signal at short times and will relatively enhance the signal at longer times, but the time-depth conversion scale will remain unchanged. We want to specify that this effect, well-known from time domain diffuse optics experimental measurement, is not evident from the model, which only provides a conversion scale from time-of-flight to the average generation depth of detected Raman photons independently of the shape of the measured time-resolved signal.

### 3.3. *CW case:* $z_{Raman}(\rho)$

The same MC simulations were also done for the CW case (SORS) for different values of source-detector distance, and in each simulation, the average generation depth of detected Raman photons was extracted. Data were then compared to the calculations from the CW extension of our model (Sec. 2.4). Figure 4 shows the results of $z_{Raman}(\rho)$ from MC simulations (solid lines) and our model (dashed lines). The corresponding probability density functions are reported in Sec. 4 of Supplement 1.

Optics EXPRESS

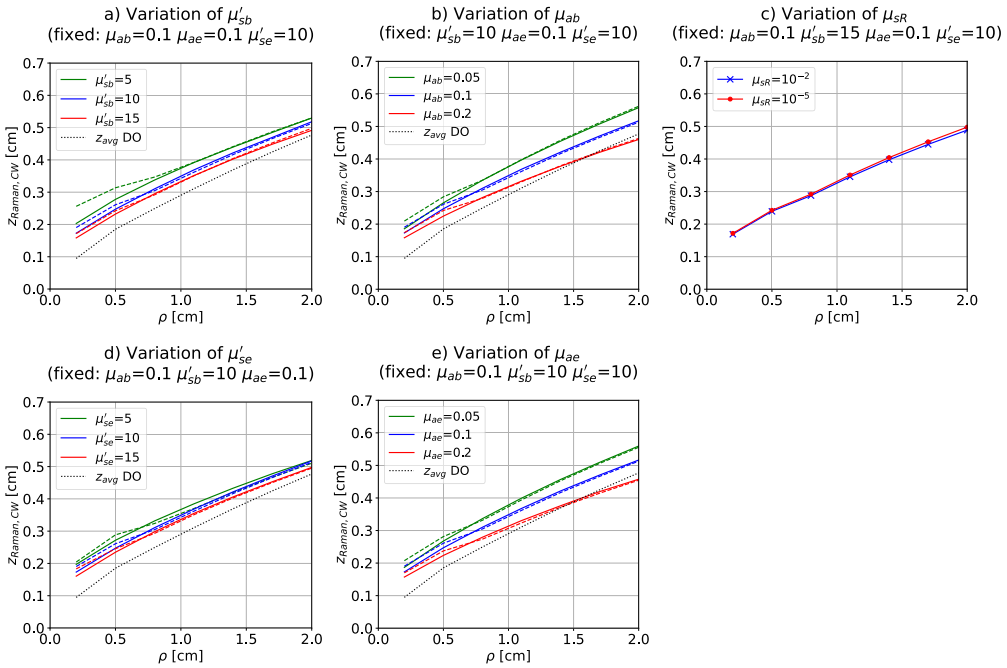


**Fig. 4.** Average generation depth (CW case) for: a) variation of $\mu'_{sb}$; b) variation of $\mu_{ab}$; c) variation of $\mu_{sR}$; d) variation of $\mu'_{se}$; e) variation of $\mu_{ae}$. The unit of optical properties is cm$^{-1}$. Solid lines refer to data from MC simulations while dashed lines to data from the model. The average depth in the case of only Tyndall scattering in a medium with $\mu_a = 0.1$ cm$^{-1}$ and $\mu'_s = 10$ cm$^{-1}$ is represented with a black dotted line. The refractive index of the medium and the external one are 1.4 and 1, respectively.

In the graphs we have also reported with a dotted black line the average photon penetration depth in the case of Tyndall diffusion at the excitation wavelength. We can note that its behavior is very similar to that of $z_{Raman}(\rho)$, as previously observed in the time domain case.

Nevertheless, we note that in the CW case, the average generation depth of detected Raman photons is weakly dependent on the optical properties of the medium. We see that $z_{Raman}(\rho)$ is barely influenced by the scattering coefficient. In particular, higher scattering slightly decreases the probed depth. While the dependence on absorption coefficient is more evident and it is clear that when absorption is higher, the average generation depth is smaller. These facts are in agreement with known effects of photon propagation in the CW regime through diffusive media.

Figure 4(c) demonstrates once again that photon propagation is independent of the Raman scattering coefficient $\mu_{sR}$, which encodes only the probability of Raman conversion of excitation photons, affecting the number of Raman photons generated, but not the way they propagate in the medium.

For small source-detector distances, the data calculated from the theoretical model begin to differ from MC simulations. However, this is expected since it is known that the Diffusion Approximation of RTE fails when $\rho$ assumes very small values. For this reason, we reported the results only for $\rho > 0.2$ cm. Also in this case, it is worth specifying that we are only giving a conversion scale from spatial offset to probed depth, without considering the reduction of signal intensity at large spatial offsets, which limits the maximum measurable depth in experimental conditions.

Optics EXPRESS

## 4. Case studies

We present here a concrete application of our theoretical model to two case studies in which we simulate the average generation depth of Raman photons for breast and arm tissues (approximately treated as homogeneous tissues), without accounting for the signal-to-noise ratio of photon arrival times. The former is pertinent to the diagnosis of breast lesions, for which SORS has been proposed as a potential technique [36]. The latter represents the detection and staging of bone osteoporosis [37]. We performed the simulations by varying the excitation wavelength in the spectral range 605-1005 nm, and for each one, we considered the optical properties recovered from a healthy volunteer [38,39]. The absorption and reduced scattering spectra are reported in Fig. 5 for the breast (blue curve) and the arm (orange curve). These results aim to gain a first idea of the generation depth in biological tissue cases without addressing the experimental limitations of this evaluation which are beyond the scope of this work.

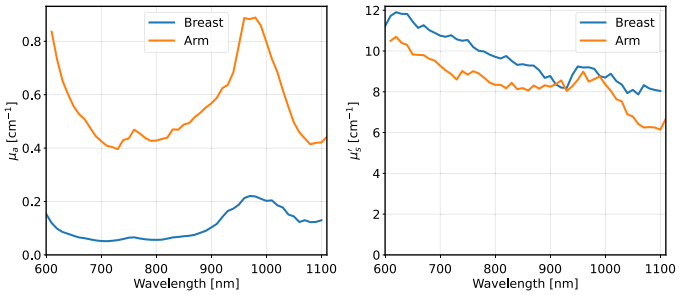


**Fig. 5.** Measured spectra of $\mu_a$ and $\mu_s'$ of breast [38] and arm [39] of a healthy volunteer, employed in the simulations.

Using the optical properties of Fig. 5, we generated $z_{Raman}(t)$ for two distinct cases: a Raman shift of 960 cm$^{-1}$ and one of 3000 cm$^{-1}$. The Raman shift of 960 cm$^{-1}$ falls inside the so-called fingerprint region and is proven to be associated with malignant calcification of apatite in breast cancer [36] or measurements of apatite concentration in bones [37]. Instead, 3000 cm$^{-1}$ is considered as an example of a large wavenumber offset that falls in between the high wavenumber region (2000 - 4000 cm$^{-1}$), where it is possible to investigate CH and OH stretching modes.

Figure 6 shows the results of our simulations: from these maps, we can see how the average generation depth strongly depends on the optical properties of the material under investigation, as expected.

Keeping the Raman shift fixed, $z_{Raman}$ increases for lower differences in absorption between excitation and emission wavelength and lower reduced scattering of the tissue. It is vital, then, to take these properties into careful consideration when modeling TD-DIRS spectra, keeping in mind their huge variability among different tissues and also among different subjects. The scope of our simulation is to optimize the depth sensitivity of a DIRS setup by fine-tuning the excitation wavelength. We observe that the commonly used 785 nm excitation wavelength is generally an optimal choice for achieving significant average generation depth in both arm and breast tissue, particularly for the 960 cm$^{-1}$ wavenumber shift. Additionally, for this wavenumber shift, an alternative optimal excitation wavelength appears to be around 930 nm. Indeed, at this wavelength, water absorption is moderate and the corresponding Raman wavelength ($\sim$ 1024 nm) falls within a region of comparable absorption. For the 3000 cm$^{-1}$ wavenumber shift, the situation is more tissue-dependent. Excitation wavelengths around 690 nm and 820 nm exhibit the highest average generation depths.

Overall, the selection of an optimal excitation wavelength should be tailored based on the wavenumber range of interest, the tissue composition, the reflectance intensity, the availability of

Optics EXPRESS

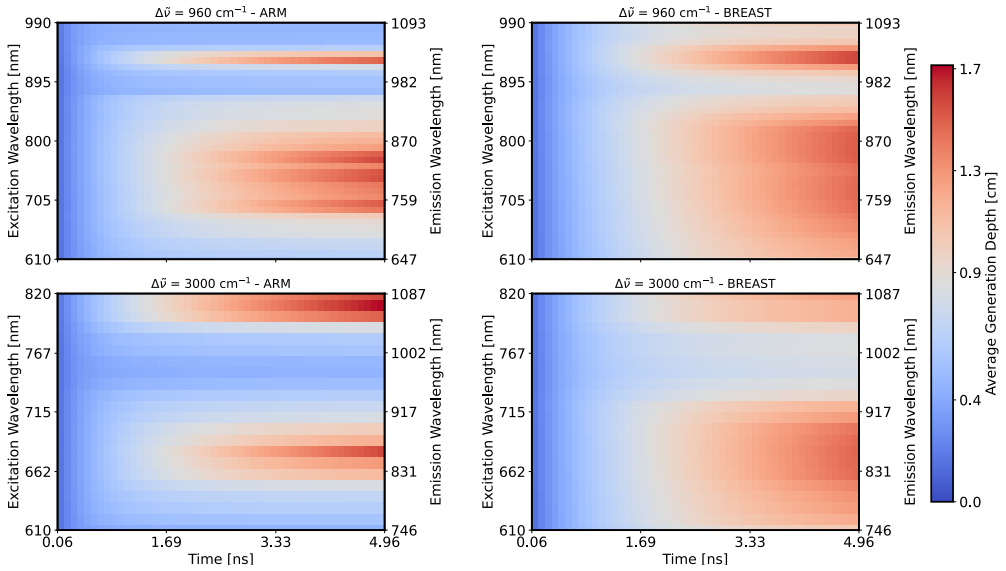


**Fig. 6.** Depth of generation simulated with different excitation wavelengths and using measured optical properties of the breast and arm of a healthy volunteer.

suitable detectors, and the need to minimize autofluorescence. Higher excitation wavelengths are particularly advantageous in reducing autofluorescence interference. This is extremely important as the autofluorescence signal covers the Raman photons, currently limiting the application of DIRS *in vivo*[8]. From our example analysis, it seems clear that for a given arrival time, using a Raman excitation around 920 nm (thus a Raman emission at wavelength > 1000 nm), holds equal, if not greater, average generation depth than using the 785 nm excitation. A practical limitation of this choice is currently the low sensitivity of silicon-based detectors. However, the growing availability of highly sensitive infrared detectors, such as InGaAs-based or superconducting nanowire detectors, could make this experimental configuration feasible. This approach is worth exploring, particularly for *in vivo* measurements.

In addition, the analysis of the average generation depth can be performed at a fixed excitation wavelength, by studying how the average depth of generation varies across a Raman spectrum as a function of the emission wavenumber. The corresponding results are provided in Sec. 6 of Supplement 1.

## 5. Conclusion

The generation depth of the Raman signal at the detector site is a critical information for many applications, as it provides insight into the chemical composition of the inner part of the medium under investigation. With this work, we have provided the basic tools and understanding of this quantity for practical use in Raman spectroscopy. Thus, the present work has been primarily focused on the calculation of the average generation depth of the Raman signal, $z_{Raman}$, from a semi-infinite homogeneous medium in time domain and CW domain. Nevertheless, the probability density function retrieved within the model enables the calculation of other quantities as well, such as the median or quartile values, that could be relevant for the interpretation of experimental measurements. To date, after previous empirical models, this is the first rigorous model describing by analytical formulas the generation depth of the detected Raman signal in diffusive media.

Optics EXPRESS

The proposed model was validated employing comparisons with the results of MC simulations for the Raman signal re-emitted from a semi-infinite homogeneous medium (Sec. 3), demonstrating good agreement for a wide set of optical properties within the typical range of near infrared spectroscopy (NIRS) applications. The main comparisons were conducted in the time domain (Fig. 3). As for the Tyndall penetration depth in the time domain, the generation depth of the Raman signal is also shown to be independent of the source-detector distance. This characteristic is essential since it reduces the parameters on which $z_{Raman}$ depends, simplifying its analysis. Afterwards, as the model can easily be extended to the CW domain, some examples were also conducted for the CW domain (Fig. 4), where, except for very short source-detector distances, the agreement was also very good. This looks promising for a following verification of the model towards experimental measurement.

The presented results show that the depth at which detected Raman photons are generated, $z_{Raman}$, can be very close to the value of the penetration depth achieved by elastically scattered photons in a diffusive medium, however, they never coincide exactly. In fact, we can imagine the Raman signal as consisting of two lives: a first Tyndall life at the excitation wavelength, and a second Raman life at the emission wavelength, under which it propagates further than the depth reached in the first part of propagation, experiencing different optical properties. This confirms the different characteristics of Raman generation and its immediate predecessor, Tyndall propagation, reinforcing the motivation of different models to describe them. This also justifies the priority given in this work to the depth of Raman generation.

Although analytical formulas for the average and maximum penetration depth of detected Raman photons ($z_{avg,Raman}$ and $z_{max,Raman}$) were not presented, they were calculated by MC simulations for all the cases analyzed in this work. The results obtained show that the simple relation $z_{max,Raman} \approx z_{avg,Raman}/2$ reasonably holds, and that a rough estimate of the value of $z_{avg,Raman}$ can be given by the value of $z_{Raman}$ calculated with the proposed model. This very preliminary result about this aspect of Raman light propagation can be the basis for future work dedicated to obtaining an analytical theory also for $z_{max,Raman}$ and $z_{avg,Raman}$.

We finally conducted simulations using the presented model and incorporating *in vivo* measured spectra of $\mu_a$ and $\mu_s'$ to estimate the probed depth in TD-DIRS measurements for different excitation wavelengths. Our findings revealed two optimal excitation wavelength regions for Raman shifts in the fingerprint region. The first is around the commonly used 785 nm, while the second one is a novel region near 920 nm, which holds significant potential for *in vivo* diffuse Raman applications due to its comparable average generation depth and substantially lower autofluorescence signal.

Although this model refers to a homogeneous geometry, using the average values of the optical properties of the bulk, it can also be used to obtain a first-order approximation of the generation depth in a heterogeneous structure, such as biological tissue often is. The approach followed constitutes a starting point for studying more complex geometries of heterogeneous media.

Our model could also be the starting point to describe the average generation depth in case of fluorescence emission inside a diffusive medium. Indeed, the modeling of fluorescence is very close to the modeling of Raman scattering, with the sole difference that the fluorescence signal is re-emitted with a time delay.

**Funding.** Ministero dell'Università e della Ricerca (2022EB4B7E[CUP B53D23002530006]); NextGenerationEU (IR0000016, ID D2B8D520, CUP B53C22001750006).

**Disclosures.** The authors declare no conflicts of interest.

**Data availability.** Data underlying the results presented in this paper are available in Ref. [40]. The code used for generating the results is available in Ref. [29] for the model, and in Ref. [35] for MC simulations.

**Supplemental document.** See Supplement 1 for supporting content.

## References

1. P. Matousek, I. P. Clark, E. R. C. Draper, *et al.*, "Subsurface probing in diffusely scattering media using spatially offset raman spectroscopy," Appl. Spectrosc. **59**(4), 393–400 (2005).

Optics EXPRESS


2. K. Sowoidnich, J. H. Churchwell, K. Buckley, *et al.*, "Photon migration of raman signal in bone as measured with spatially offset raman spectroscopy," J. Raman Spectrosc. **47**(2), 240–247 (2016).
3. S. Mosca, C. Conti, N. Stone, *et al.*, "Spatially offset raman spectroscopy," Nat. Rev. Methods Primers **1**(1), 21 (2021).
4. S. K. V. Sekar, S. Mosca, A. Farina, *et al.*, "Frequency offset raman spectroscopy (fors) for depth probing of diffusive media," Opt. Express **25**(5), 4585–4597 (2017).
5. P. Matousek and A. W. Parker, "Bulk raman analysis of pharmaceutical tablets," Appl. Spectrosc. **60**(12), 1353–1357 (2006).
6. K. Buckley and P. Matousek, "Recent advances in the application of transmission raman spectroscopy to pharmaceutical analysis," J. Pharm. Biomed. Anal. **55**(4), 645–652 (2011).
7. S. K. V. Sekar, S. Mosca, S. Tannert, *et al.*, "Time domain diffuse raman spectrometer based on a tcspc camera for the depth analysis of diffusive media," Opt. Lett. **43**(9), 2134–2137 (2018).
8. A. Bossi, S. K. V. Sekar, M. Lacerenza, *et al.*, "Time domain diffuse raman spectroscopy using single pixel detection," Biomed. Opt. Express **14**(11), 5749–5763 (2023).
9. S. Šušnjar, F. Martelli, S. Mosca, *et al.*, "Two-layer reconstruction of raman spectra in diffusive media based on an analytical model in the time domain," Opt. Express **31**(24), 40573–40591 (2023).
10. F. Nicolson, B. Andreiuk, C. Andreou, *et al.*, "Non-invasive in vivo imaging of cancer using surface-enhanced spatially offset raman spectroscopy (sesors)," Theranostics **9**(20), 5899–5913 (2019).
11. A. Ghita, P. Matousek, and N. Stone, "High sensitivity non-invasive detection of calcifications deep inside biological tissue using transmission raman spectroscopy," J. Biophotonics **11**(1), e201600260 (2018).
12. K. Sowoidnich, J. H. Churchwell, K. Buckley, *et al.*, "Spatially offset raman spectroscopy for photon migration studies in bones with different mineralization levels," Analyst **142**(17), 3219–3226 (2017).
13. C. Shu, K. Chen, M. Lynch, *et al.*, "Spatially offset raman spectroscopy for in vivo bone strength prediction," Biomed. Opt. Express **9**(10), 4781–4791 (2018).
14. W. J. Olds, E. Jaatinen, P. Fredericks, *et al.*, "Spatially offset raman spectroscopy (sors) for the analysis and detection of packaged pharmaceuticals and concealed drugs," Forensic Sci. Int. **212**(1-3), 69–77 (2011).
15. C. Conti, C. Colombo, M. Realini, *et al.*, "Subsurface analysis of painted sculptures and plasters using micrometre-scale spatially offset raman spectroscopy (micro-sors)," J. Raman Spectrosc. **46**(5), 476–482 (2015).
16. J. Johansson, S. Pettersson, and S. Folestad, "Characterization of different laser irradiation methods for quantitative raman tablet assessment," J. Pharm. Biomed. Anal. **39**(3-4), 510–516 (2005).
17. D. Yang and Y. Ying, "Applications of raman spectroscopy in agricultural products and food analysis: A review," Appl. Spectrosc. Rev. **46**(7), 539–560 (2011).
18. A. H. Gandjbakhche and G. H. Weiss, "Descriptive parameter for photon trajectories in a turbid medium," Phys. Rev. E **61**(6), 6958–6962 (2000).
19. F. Martelli, T. Binzoni, A. Pifferi, *et al.*, "There's plenty of light at the bottom: statistics of photon penetration depth in random media," Sci. Rep. **6**(1), 27057 (2016).
20. F. Martelli, T. Binzoni, S. Del Bianco, *et al.*, *Light Propagation Through Biological Tissue and Other Diffusive Media: Theory, Solutions, and Validation* (SPIE, 2022).
21. F. Martelli, A. Pifferi, A. Farina, *et al.*, "Statistics of maximum photon penetration depth in a two-layer diffusive medium," Biomed. Opt. Express **15**(2), 1163–1180 (2024).
22. N. Everall, T. Hahn, P. Matousek, *et al.*, "Photon migration in raman spectroscopy," Appl. Spectrosc. **58**(5), 591–597 (2004).
23. S. Mosca, P. Dey, M. Salimi, *et al.*, "Spatially offset raman spectroscopy - how deep?" Anal. Chem. **93**(17), 6755–6762 (2021).
24. F. Martelli, T. Binzoni, S. K. V. Sekar, *et al.*, "Time-domain raman analytical forward solvers," Opt. Express **24**(18), 20382–20399 (2016).
25. R. Re, L. Spinelli, F. Martelli, *et al.*, "A review on time domain diffuse optics: principles and applications on human biological tissues," Riv. Nuovo Cim. **48**(3), 157–239 (2025).
26. F. Martelli, S. Del Bianco, A. Ismaelli, *et al.*, *Light propagation through biological tissue and other diffusive media: theory, solutions, and software* (SPIE, 2009).
27. P. Virtanen, R. Gommers, T. E. Oliphant, *et al.*, "SciPy 1.0: Fundamental Algorithms for Scientific Computing in Python," Nat. Methods **17**(3), 261–272 (2020).
28. D. Contini, F. Martelli, and G. Zaccanti, "Photon migration through a turbid slab described by a model based on diffusion approximation. i. theory," Appl. Opt. **36**(19), 4587–4599 (1997).
29. A. Bossi and V. Gandolfi, "Raman-depth," GitHub (2025), https://github.com/alebossi96/Raman-depth.
30. S. Del Bianco, F. Martelli, F. Cignini, *et al.*, "Liquid phantom for investigating light propagation through layered diffusive media," Opt. Express **12**(10), 2102–2111 (2004).
31. N. Everall, P. Matousek, N. MacLeod, *et al.*, "Temporal and spatial resolution in transmission raman spectroscopy," Appl. Spectrosc. **64**(1), 52–60 (2010).
32. F. Foschum and A. Kienle, "Optimized goniometer for determination of the scattering phase function of suspended particles: simulations and measurements," J. Biomed. Opt. **18**(8), 085002 (2013).
33. L. Wang, S. L. Jacques, and L. Zheng, "Mcml-monte carlo modeling of light transport in multi-layered tissues," Computer Methods and Programs in Biomedicine **47**(2), 131–146 (1995).

Optics EXPRESS


34. E. Alerstam, W. C. Y. Lo, T. D. Han, *et al.*, "Next-generation acceleration and code optimization for light transport in turbid media using gpus," Biomed. Opt. Express **1**(2), 658–675 (2010).
35. A. Farina, "Mc-cuda-raman," GitHub (2025), https://github.com/andreafarina/MC-CUDA-RAMAN.
36. N. Stone, R. Baker, K. Rogers, *et al.*, "Subsurface probing of calcifications with spatially offset raman spectroscopy (sors): future possibilities for the diagnosis of breast cancer," Analyst **132**(9), 899–905 (2007).
37. G. Feng, M. Ochoa, J. R. Maher, *et al.*, "Sensitivity of spatially offset raman spectroscopy (sors) to subcortical bone tissue," J. Biophotonics **10**(8), 990–996 (2017).
38. N. Serra, R. Cubeddu, G. Maffeis, *et al.*, "In vivo optimization of the experimental conditions for the non-invasive optical assessment of breast density," Sci. Rep. **14**(1), 19154 (2024).
39. I. Bargigia, S. Karremans, V. Damagatla, *et al.*, "Comprehensive dataset of absorption and scattering spectra of in-vivo biological tissues using time-domain diffuse optical spectroscopy," *Optical Tomography and Spectroscopy* (Optica Publishing Group, 2024), paper OS3D–8.
40. A. Bossi, V. Gandolfi, A. Farina, *et al.*, "Dataset for "Generation depth modeling in time-domain diffuse Raman spectroscopy: the homogeneous case"," Zenodo (2025), https://doi.org/10.5281/zenodo.15685690.